Materials International
Open Access Journal (ISSN: 2668-5728)

Article
Volume 7, Issue 1, 2025, 6
https://doi.org/10.33263/Materials71.006

Structure and Characterization of $Gd_2O_3/SnO_2/Fe_2O_3$ Nanocomposites for Electrical Conductivity, Optical, and Photocatalytic Investigations

Namitha P.V. [1], Kusuma Y.M. [1], Mohammed Shibli K.A. [1], Ramesh S [1], Yukthi D.M. [1,*]

[1] School of Physical Sciences, Amrita Vishwa Vidyapeetham, Mysuru Campus, Mysuru – 570 026, Karnataka, India
* Correspondence: yukthiyukz432@gmail.com;

Scopus Author ID -
Received: 30.08.2024; Accepted: 2.01.2025; Published: 13.02.2025

Abstract: In this work, we report the preparation and characterization of $Gd_2O_3/SnO_2/Fe_2O_3$ nanocomposites using the sol-gel method. The as-prepared nanomaterials were characterized using powder X-ray diffraction (PXRD), scanning electron microscopy (SEM), UV-visible spectroscopy, and diffuse reflectance spectra (DRS) techniques. The XRD pattern reveals the average crystallite size of the as-prepared $Gd_2O_3/SnO_2/Fe_2O_3$ nanocomposites is 21.9 nm. Further, the SEM analysis of the as-prepared sample shows planar and rod-like irregularly shaped nanoparticles, and the small ball-like particles were decorated on the surface of the samples, which confirms that the three different samples were present and mixed throughout the sample, further confirming that there exist three different materials in the sample. Furthermore, the dielectric properties, AC electrical studies, and impedance analysis of the individual components (Fe_2O_3, Gd_2O_3, SnO_2) and the nanocomposite ($SnO_2/Gd_2O_3/Fe_2O_3$) were examined by dielectric studies. The results revealed that the grain boundaries were more resistive than those of grains due to disordered atomic arrangements near the grain boundaries, enhancing electron scattering and increasing resistivity. The composite of $SnO_2/Gd_2O_3/Fe_2O_3$ demonstrated a superior dielectric function compared to the separate materials, indicating its potential for energy harvesting applications. The photocatalytic Investigations of the $SnO_2/Gd_2O_3/Fe_2O_3$ composite's capacity to break down methylene blue (MB) dye under light exposure was assessed to determine its photocatalytic activity.

Keywords: $Gd_2O_3/SnO_2/Fe_2O_3$ nanocomposites; PXRD; DRS; dielectric studies.

1. Introduction

The rising energy demand and accompanying environmental problems have stimulated considerable interest in developing technologies harnessing renewable energy sources. Among these, solar energy stands out as a promising path for efficient energy conversion, with hydrogen production emerging as a pivotal application. Sunlight is a potent energy source, as photovoltaics and photocatalysis have converted solar energy to electric energy and chemical reactions [1,2]. The photovoltaics have accelerated electricity generation by speeding up electron movement within solar cells. Solar farms represent a significant stride towards reducing dependence on fossil fuels while boosting energy security. Moreover, solar power holds immense potential for decarbonizing industries and mitigating energy costs, particularly in mining sectors that often rely on diesel generators in remote regions. Like vice, the

photocatalytic materials observe the sunlight and undergo the advanced oxidation process for wastewater degradation.

Numerous strategies have been developed to overcome the drawbacks, such as bandgap engineering, through heterostructure construction. A detailed study in this avenue has revealed that the proper energy band alignments across two semiconductors' interfaces can effectively improve charge separation by crippling the photogenerated electron-hole pairs' recombination. Various approaches have been examined to enhance the photocatalytic activity of materials. Some of these approaches include doping, surface modification, the production of composites, and heterostructure assembly. Amongst heterostructure designs, one has attracted much attention because of its capacity to facilitate the combing of several phases, ultimately resulting in improved catalytic activities. In heterostructures, the interaction between different metals makes charge transfer easier, ultimately increasing the catalytic process's effectiveness [3,4].

The heterostructure, photo, and electrocatalyst demonstrate that the synergistic interaction of multiple metals boosts charge transfer and enhances catalytic activity. Wang employed CoMo LDH as a template after dissolution regeneration, followed by annealing and salinization to create $MoSe_2/Co_{0.85}$-Se heterostructures with outstanding electrocatalytic activity. Zhon used stainless steel mesh as a substrate to load NiCo LDH, followed by subsequent hydrothermal treatment, to successfully produce a $CoSe/Ni_3Se_4$ heterostructure that exposed more active sites, lowered charge transfer resistance, and performed well in electrocatalytic hydrolysis [5]. Hashem et al. investigated the single-phase structures of SnO_2 and ZnO, and the significance of oxygen vacancies improved the efficiency. Similarly, bi-metal oxide heterostructures such as NiO/TiO_2, Fe_2Se_3/Fe_2O_3, and TiO_2/MO (Co_3O_4, Fe_2O_3, Fe_3O_4, and CuO) are also proven excellent candidates for the electro and photocatalytic applications [6].

Iron oxide (Fe_2O_3) is a transition metal oxide with varying stoichiometric and crystalline structures, including wurtzite (FeO), hematite (α Fe_2O_3), maghematite (v Fe_2O_3), and magnetite (Fe_3O_4). Hematite (Fe_2O_3) is the most stable form of iron oxide at ambient temperatures. Fe_2O_3 is one of the most appealing materials for PEC (photoelectrochemical) due to its favorable band gap (2.1 eV), high stability in aqueous solution, non-toxicity, and abundant availability. The SnO_2 is another essential material because it and structures with varied morphologies interact to generate inherent defects and contribute to defect-induced ferromagnetism. SnO_2 has attracted much attention due to its large surface area, which allows for efficient catalytic reactions. SnO_2, in particular, has various distinguishing characteristics that set it apart from other materials.

First and foremost, SnO_2 is an environmentally friendly, non-toxic substitute for other dangerous elements. Second, the SnO_2 application involves photocatalysis sensing energy conversion optical and electrical properties, such as high surface area and vital stability broadband gap (3.6 eV). Gd_2O_3 is a rare earth oxide and an exciting compound in numerous applications such as microelectronics, optoelectronics, and optical devices due to its intriguing electronic configuration (Gd; [Xe] 4f7 5d1 6s Half-filled 4f and partly filled 5d orbitals) and high refractive index, presenting Gd_2O_3 as a valuable optical substance. Its high relative permittivity, high resistivity, and enormous gap are attractive for high-technology applications.

The binary heterostructures of the Fe_2O_3/SnO_2, CeO_2/SnO_2, NiO/SnO_2, Fe_2O_3/ Fe_3O_4, Fe_2O_3/ZnO, CdS/ Fe_2O_3, CdS/Gd_2O_3, CuO/ Gd_2O_3, CuO/Ti_3C_2, $Bi2O_3/SiO_2$, ZnSe/SnO Fe2O3/Gd2O3 has proven their enhanced performance through the rapid separation and slow recombination of photoinduced electron-hole pairs. A mechanism is presented to explain the

increased visible-light photocatalytic activity. In recent time times, there have been several reports on ternary metal oxides heterostructure fabrications such as $NiFe_2O_4/BiVO_4/Bi_2MoO_6$, $Mg_3V_2O_8/Zn_3V_2O_8$, Au/ZnO/rGO, $Pt/BaTiO_3$, $NiO/MoS_2/BiVO_4$, $Fe2O_3$ / Fe_3O_4/CdS, Gd_2O_3/ Fe_2O_3/ CoO, ZnO/MnO_2/ Gd_2O_3 and the quaternary $BiOCl/gCN/Fe_3O_4/Cu_2O$ heterojunction have shown 99.5 % degradation of selected contaminant in 1 h and 92 % removal of contaminant under sunlight radiation of 2 h [7].

Based on the above facts, in this work, we design and synthesize the ternary α-$Fe_2O_3/Gd_2O_3/SnO_2$ heterostructure composite by sol-gel method and investigate their structural, morphological, electrical, electrochemical, conductivity, and magnetic properties for multifunctional applications.

2. Materials and Methods

2.1. Materials and methods.

Reagent-grade chemicals $Fe(NO_3)_3$ x $9H_2O$ [Avra; 98% purity; M.W 404 g/mol, $SnCl_2$ [Rankem; 95%purity; M.W 225.65 g/mol], Gd_2O_3, [CDH; 99.9% purity; M.W 362.50 g/mol] Citric acid and HNO_3 were used throughout the synthesis without further purification. The phase purity of the material was analyzed using a Powder X-ray diffractometer (Bruker). The surface morphology was investigated using a Zeiss scanning electron microscope (Japan). Electrical conductance was measured on a Glassco conductivity meter having a cell with cell constant 1. Dye degradation studies were carried out using a photocatalytic reactor (REMI, India). Absorption studies were performed using a UV-visible spectrophotometer (UV-3200 Lab India, India).

2.2. Synthesis of Fe_2O_3 nanoparticles.

The Fe_2O_3 nanoparticles were prepared using the sol-gel technique. The calculated amount of $Fe(NO_3)_3$ x $9H_2O$ (4.04 g) was added to the distilled water to make 0.1 M solution, and then 50 mL of 0.5 mol/L citric acid solution was added. The pH 6 of the solution was maintained using liquid ammonia (20 %). The above resulting solution turns into a pale yellow solution. This was then stirred continuously using a magnetic stirrer at 60°C until it became a transparent gel. The gel thus obtained was dried in the heating mantle at 120°C for 1 hour, which led to the formation of lightweight porous materials. This was further calcinated at 800°C for 8 hours for a fine, homogenous, dense powder.

2.3. Synthesis of SnO_2 nanoparticles.

The SnO_2 particles were prepared using the sol-gel method. The calculated amount (5.088g) of $SnCl_2$ is dissolved in concentrated HNO_3 (15 mL), followed by adding 50 mL of 0.5 mol/L citric acid solution. Then, the same conditions were followed as in the above case.

2.4. Synthesis of Gd_2O_3.

The Gd_2O_3 particles were prepared using the sol-gel method. The calculated amount (0.946 g) of Gd_2O_3 was converted to $Gd_2(NO_3)_3$ by adding concentrated HNO_3, followed by the addition of 50 mL of 0.5 mol/L citric acid solution. Then, the same conditions were followed as in the above case.

2.5. Synthesis of $Fe_2O_3/Gd_2O_3/SnO_2$ heterostructure nanocomposites.

All the metal oxide nanoparticles obtained above were mixed with ethanol and stirred well for one hour to obtain a homogenous mixture. Thus, the obtained material was dried at 300°C, yielding the final product of $Gd_2O_3/SnO_2/Fe_2O_3$ heterostructure nanocomposites.

3. Results and Discussion

3.1. X-ray diffraction analyses.

Figure 1 shows the XRD pattern of the as-prepared $SnO_2/Gd_2O_3/Fe_2O_3$ composite, which is compared with the experimentally obtained individual nanomaterials, SnO_2, Gd_2O_3, and Fe_2O_3. All three individual material patterns match the composite PXRD patterns, which confirms that the three phases are present in the composites. No other additional peaks were identified, which reveals that the samples do not have any other impurities or phases.

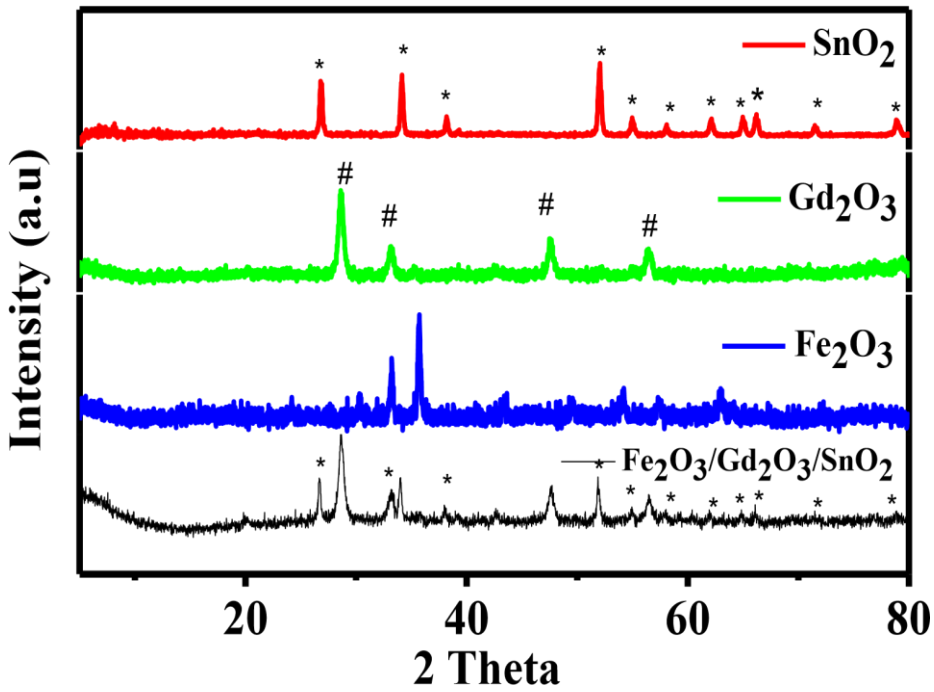

Figure 1. Powder X-ray diffraction patterns of the $SnO_2/Gd_2O_3/Fe_2O_3$ nanocomposites compared with the individual SnO_2, Gd_2O_3, and Fe_2O_3 nanomaterials.

The average crystalline sizes (D) of all PXRD (SnO_2, Gd_2O_3, and Fe_2O_3 and composites) were estimated using the Scherrer equation [1]:

$$crystalline\ size\ (D) = \frac{0.9\lambda}{B_{hkl}\cos\theta} \qquad (1)$$

Where 0.9 is the shape factor, λ, B_{hkl}, and θ being the wavelength of the x-rays used, full-width half maximum (FWHM), and diffracting angle, respectively. The estimated crystalline sizes of the samples are listed in Table 1.

Table 1. Particle size of the SnO_2/ Gd_2O_3/Fe_2O_3 nanocomposites.

Pos. [2θ]	FWHM left [2θ]	Size (nm)
26.8354	0.3149	27.138
28.6442	0.3936	21.797
33.1984	0.4723	18.366
35.2735	0.4723	18.468
40.9274	0.4723	18.786
42.7103	0 .9446	9.449

Pos. [2θ]	FWHM left [2θ]	Size (nm)
47.5907	0.3936	23.093
49.5290	0.4723	19.384
52.0243	0.3149	29.375
56.3792	0.3936	23.963
64.1006	0.3149	31.148
Average crystallite size		21.906

3.2. UV-visible spectroscopy.

The UV–Vis–NIR diffuse reflectance spectra (DRS) of Fe_2O_3 material were obtained in the range of 200–800 nm (Figure 2a). A strong band observed between 700 and 750 nm is attributed to the charge transfer band (CTB), which is a band that moves from the O^{2-} ligand to the Metal in the host lattice. The optical bandgap energy is generally determined from measured diffuse reflectance spectra, which can be transformed into the corresponding absorption spectra by applying Kubelka–Munk equation and Tauc plot (Figure 2b) [8-11]. Although the K-M plot and the Tauc plot both evaluate the interaction between light and materials, the K-M plot is superior when it comes to materials that are opaque or scatter light and homogenous samples. When compared to Tauc plots, K-M plots are less susceptible to the effects of scattering and provide a more comprehensive picture since they consider both the effects of absorption and scattering. Because of this, K-M is a more suitable option for comprehending the entire light interaction in samples of this kind (Figure 2c) [12].

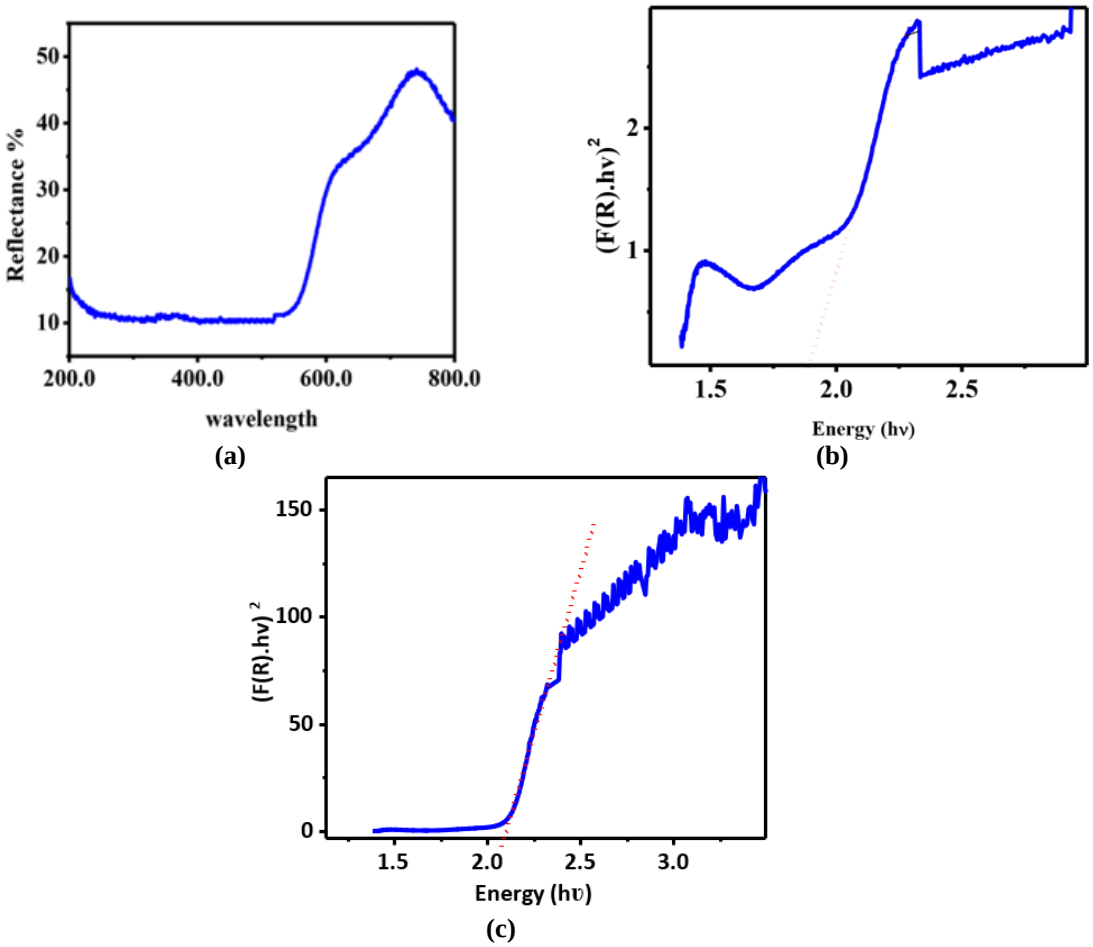

Figure 2. (a) DRS spectrum at room temperature; **(b)** Kubelka-Munk direct bandgap; **(c)** indirect bandgap of the SnO_2/ Gd_2O_3/Fe_2O_3 nanocomposites.

3.3. Morphological studies.

The scanning electron microscopy (SEM) images of the $SnO_2/Gd_2O_3/Fe_2O_3$ nanocomposites are shown in Figure 3. The sample shows planar and rod-like irregularly shaped nanoparticles, and the small ball-like particles were decorated on the surface of the samples, which confirms that the three different samples were present and mixed throughout the sample. The calculated size of the material ranges between 9 and 31 nm, which is in good agreement with the X-ray diffraction results.

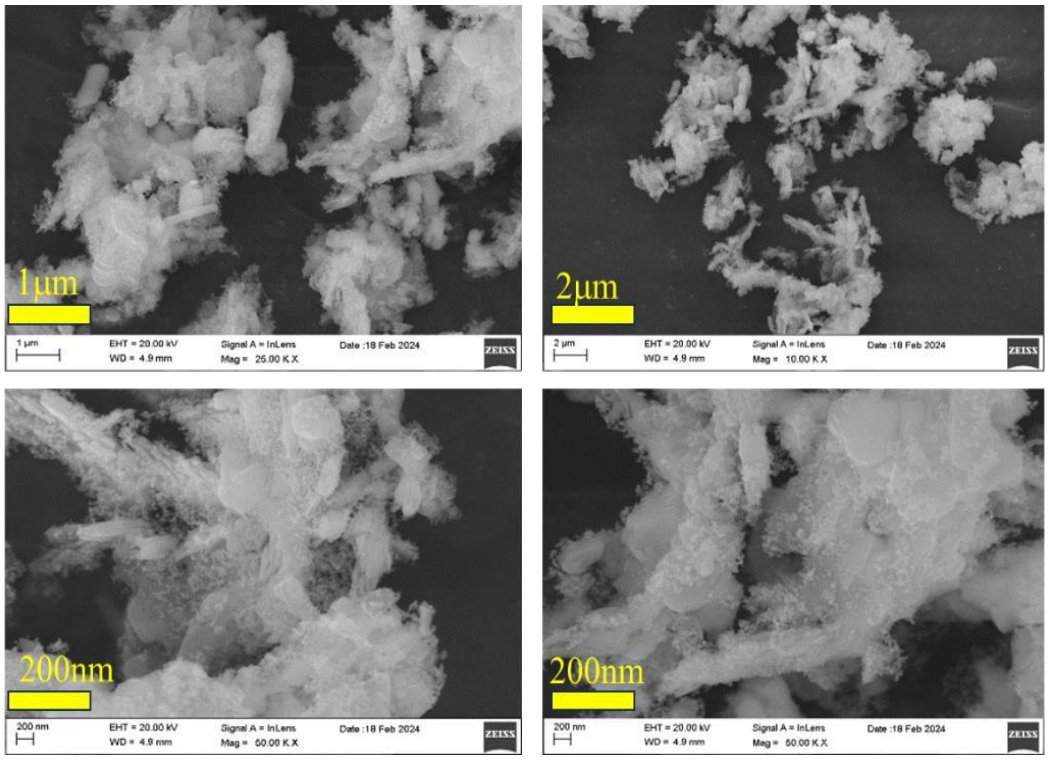

Figure 3. SEM images of as-prepared $SnO_2/Gd_2O_3/Fe_2O_3$ nanocomposites.

3.4. Conductivity studies.

3.4.1. Impedance analysis.

Figures 4(a-c) show the real, imaginary, and Nyquist plots of the Fe_2O_3, Gd_2O_3, SnO_2, and $SnO_2/Gd_2O_3/Fe_2O_3$ samples. It is observed that the decrease in real (Z') and imaginary (Z") parts of impedance with respect to the frequency increases. As in the tan δ case, different conduction mechanisms are involved in the wide range of the frequency range. As previously stated [13], numerous oxide materials consist of polar molecules or ionic defects. These dipoles attempt to orient themselves in accordance with the direction of the electric field. At lower frequencies, the dipoles experience an extended time of reorienting themselves or trapping the charge, which obstructs the movement of electric current and results in increased resistance, including both the real and imaginary components. At elevated frequencies, the dipoles experience less reorientation capability, resulting in diminished obstruction to current flow, a decline in impedance, and enhanced conduction due to the hopping of electrons between the localized ions.

Additionally, the grain and the grain boundaries affect the polycrystalline materials. In high-frequency regions, both Z' and Z" become independent of frequency. The composite materials show less impedance than the Fe_2O_3, which becomes flat at a high frequency [14].

A Nyquist plot displays the imaginary component of impedance (Z") on the y-axis and the real component (Z') on the x-axis across a range of frequencies. The impedance of oxide composites often exhibits a drop in its real and imaginary components as the frequency increases. This behavior can be attributed to factors such as dielectric relaxation and capacitive reactance, as previously explained. This leads to the formation of a curve that is either semi-circular or elliptical on the Nyquist plot. Figure 4(c) shows the elliptical nature of responses, which leads to the observation of the presence of multiple relaxation processes. According to the heterogeneous two-layered model, polycrystalline materials are composed of grains separated by grain boundaries. Grain boundaries are more resistive than grains due to disordered atomic arrangements near the grain boundaries, which enhance electron scattering and result in increased resistivity. It is reported that the electrical properties of ferrites are controlled mainly by grain boundaries. It is well known that the larger the crystallite size, the lesser the number of grain boundaries and vice versa [15].

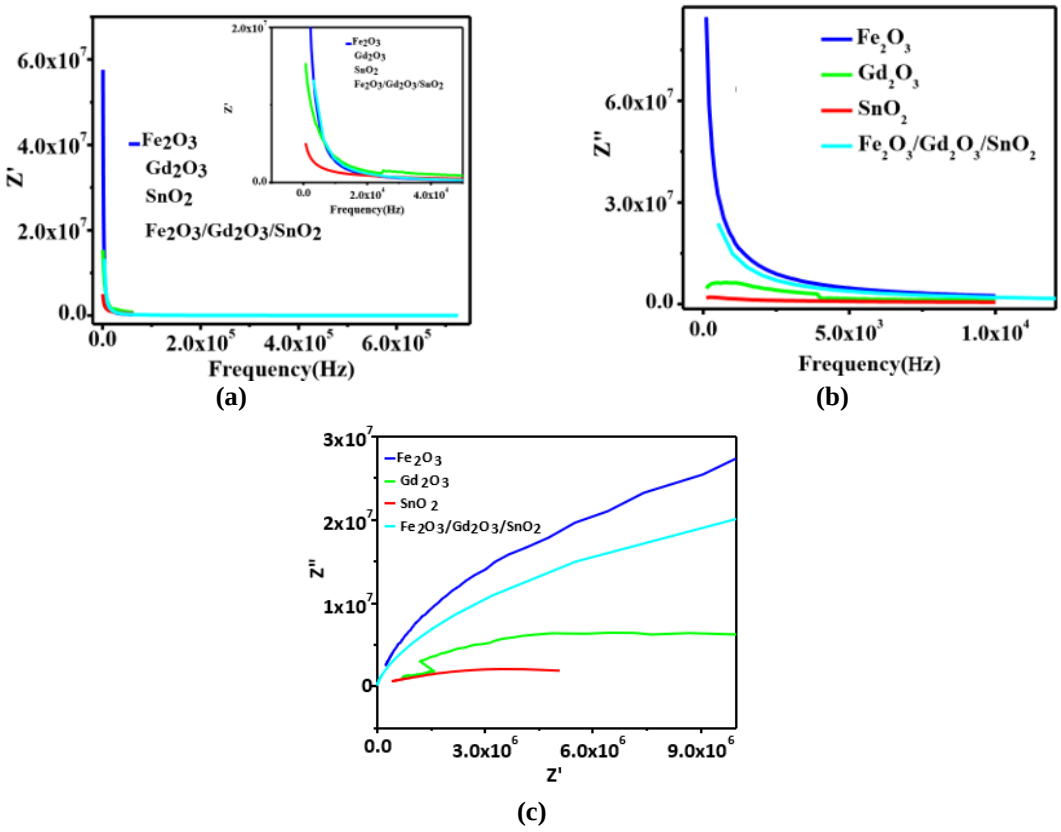

Figure 4. Frequency dependent Impedance **(a)** real part; **(b)** imaginary part; **(c)** Nyquist plots of the Fe_2O_3, Gd_2O_3, SnO_2 and $SnO_2/Gd_2O_3/Fe_2O_3$ nanocomposites.

3.4.2. AC conductivity.

The AC conductivity of the as-prepared nanocomposites was determined by measuring the dielectric properties of the materials (Figure 5). The increased conductivity associated with the higher frequencies can be ascribed to charge carriers that are confined to certain regions. When the frequency is low, the conductivity spectrum may be extrapolated to obtain the dc conductivity (σ_{dc}), which is caused by the charge carriers' long-range translational motion. At higher frequencies, the dc conductivity (σ_{ac} (ω) exhibits dispersion and increases, which follows Jonscher's power law [16]. This power law, also referred to as universal power law, is employed to characterize the materials' electrical conductivity (σ) varies with frequency. Using

the Jonscher's power law fit, we calculated the conductivity according to the relation given below in equation 2:

$$S_{a.c} = S_{d.c} + A\omega^s \qquad (2)$$

Where $S_{a.c}$ represents the Ac conductivity, $S_{d.c}$ represents the material's conductivity when a constant electric field is applied. $A\omega^s$ refers to the frequency-dependent behavior of the conductivity.

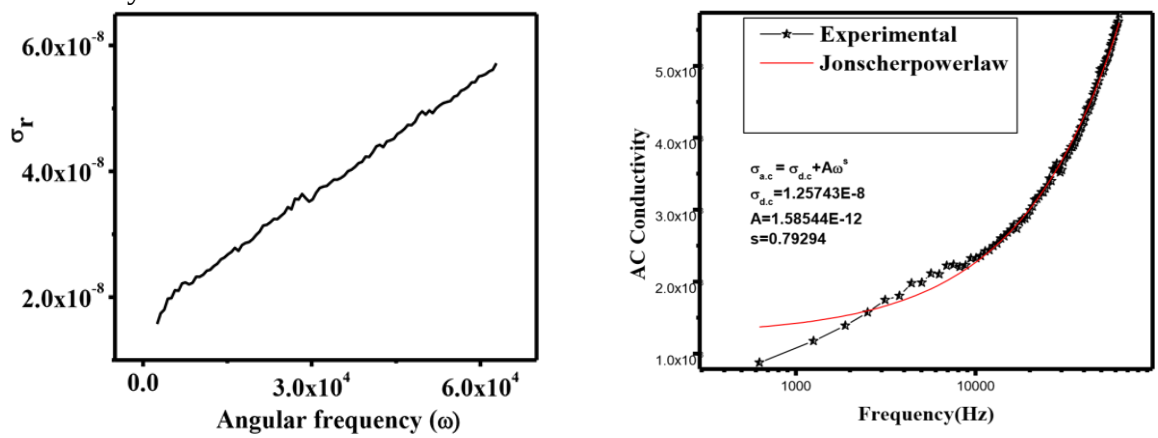

Figure 5. (a) Frequency-dependent conductivity; **(b)** Jonscher power law fitting of the $Gd_2O_3/SnO_2/Fe_2O_3$ nanocomposites.

The calculated $s_{d.c}$, A, and s values are 2.25743E-8, 1.58544E-12, and 0.79294. The σ_{ac} increase in frequency results in enhanced conductivity, indicating that the frequency facilitates the hopping of the charge carriers between Fe^{2+} ions [17].

3.5. Photocatalytic studies.

The as-prepared nanocomposites were assessed for their photocatalytic activity by degrading methylene blue (MB) dye. Photodegradation studies were carried out under 150W tungsten halogen lamps as the light source. At different intervals (0, 15, 30, 45, 60, and 75 minutes), portions of the solution containing MB dye and as-prepared nanocomposites were taken and centrifuged at 5000 rotations per minute for 5 minutes. The resulting solutions were further analyzed using a UV–visible spectrophotometer to examine the photocatalytic process further. It is evident from Figure 6 that the degradation has occurred in a time-dependent manner. At the 60th minute, the absorption showed significant photocatalytic dye degradation [18]. Further, no degradation was observed after this time.

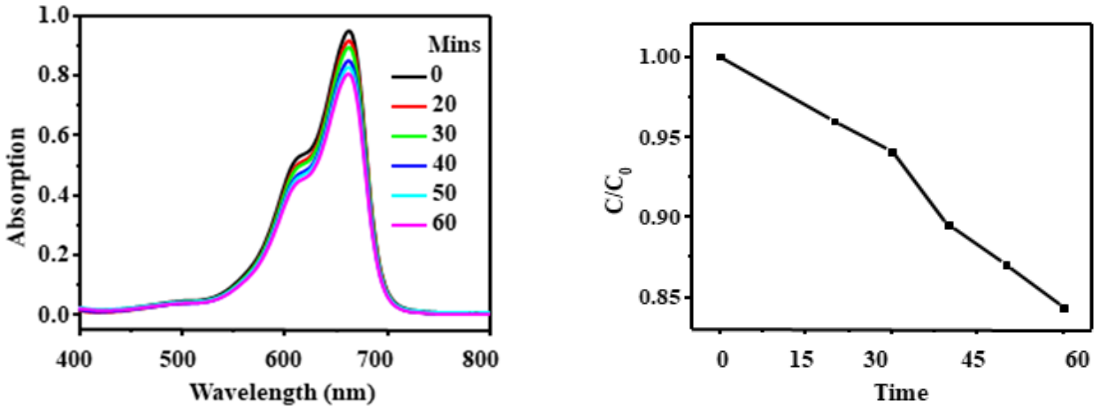

Figure 6. (a) Time-dependent absorption spectrum of methylene blue dye in the presence of as-prepared $Gd_2O_3/SnO_2/Fe_2O_3$ nanocomposites; **(b)** Decrement of MB dye concentration against time.

4. Conclusion

To sum up, pure samples of Fe_2O_3, Gd_2O_3, SnO_2, and a composite material combining $SnO_2/Gd_2O_3/Fe_2O_3$ were successfully synthesized and thoroughly investigated for their structural, morphological, optical, and conductivity properties, with potential applications in photodegradation. X-ray diffraction analysis confirmed the crystalline structure and phases present in each constituent material of the composite. The average crystallite size of the nanoparticles was 21.9 nm. The semiconductor characteristics of the composite were determined by analyzing its optical band gap through UV-visible spectroscopy, employing the Kubelka-Munk method. SEM analysis showed the existence of flat and rod-shaped nanoparticles with uneven shapes, as well as small spherical particles. This suggests that the composite sample has a mixture of three different materials. The AC electrical studies and impedance analysis of the individual components (Fe_2O_3, Gd_2O_3, SnO_2) and the composite ($SnO_2/Gd_2O_3/Fe_2O_3$) were examined, which demonstrated that the composite of $SnO_2/Gd_2O_3/Fe_2O_3$ exhibits superior dielectric function in comparison to the individual materials, indicating its potential for use in energy harvesting applications. The photocatalytic investigations of as-prepared $SnO_2/Gd_2O_3/Fe_2O_3$ composites' capacity to break down methylene blue (MB) dye under light exposure were assessed to determine its photocatalytic activity. The results revealed that the as-prepared nanocomposites showed significant efficiency in degrading the dye.

Funding

The author declares that they have no known competing financial interests that could have appeared to influence the work reported in this paper.

Acknowledgments

Authors extend their appreciation to the Director, Amrita Vishwa Vidyapeetham, Mysuru Campus, for providing instrumentation and infrastructure facilities.

Conflicts of Interest

The author declares that they have no known personal relationships that could have appeared to influence the work reported in this paper.

References

1. Lavín, A.; Sivasamy, R.; Mosquera, E.; Morel, M.J. High proportion ZnO/CuO nanocomposites: Synthesis, structural and optical properties, and their photocatalytic behavior. *Surfaces and Interfaces* **2019**, *17*, 100367, https://doi.org/10.1016/j.surfin.2019.100367.
2. Sivasamy, R.; Venugopal, P.; Mosquera, E. Synthesis of Gd_2O_3/CdO composite by sol-gel method: Structural, morphological, optical, electrochemical and magnetic studies. *Vacuum* **2020**, *175*, 109255, https://doi.org/10.1016/j.vacuum.2020.109255.
3. Zhang, L.F.; Zhu, J.T.; Wang, Z.; Zhang, W.J. 2D $MoSe_2$/CoP intercalated nanosheets for efficient electrocatalytic hydrogen production. *Int. J. Hydrog. Energy* **2020**, *45*, 19246-19256, https://doi.org/10.1016/j.ijhydene.2020.05.059.
4. Zheng, G.; Wang, J.; Zu, G.; Che, H.; Lai, C.; Li, H.; Murugadoss, V.; Yan, C.; Fan, J.; Guo, Z. Sandwich structured WO_3 nanoplatelets for highly efficient photoelectrochemical water splitting. *Journal of Materials Chemistry A* **2019**, *7*, 26077-26088, https://doi.org/10.1039/C9TA09188B.

5. Zheng, Y.; Zhang, H.; Xiong, J.; Zhao, Z.; Zhang, D.; Chen, L. Anion-induced vacancy enhances Co_3Se_4/Fe_3Se_4 heterostructures for high-efficiency hydrogen production. *Fuel* **2024**, *360*, 130651, https://doi.org/10.1016/j.fuel.2023.130651.
6. Sharma, S.; Kumar, N.; Makgwane, P.R.; Chauhan, N.S.; Kumari, K.; Rani, M.; Maken, S. TiO_2/SnO_2 nano-composite: New insights in synthetic, structural, optical and photocatalytic aspects. *Inorganica Chimica Acta* **2022**, *529*, 120640, https://doi.org/10.1016/j.ica.2021.120640.
7. Xu, H.; Li, W.; Han, R.; Zhai, T.; Yu, H.; Chen, Z.; Wu, X.; Wang, J.; Cao, B. Enhanced triethylamine sensing properties by fabricating $Au@SnO_2/\alpha\text{-}Fe_2O_3$ core shell nanoneedles directly on alumina tubes. *Sensors and Actuators* **2018**, *262*, 70-78, https://doi.org/10.1016/j.snb.2018.01.209.
8. Majani, S.S.; Basavaraj, R.B.; Iqbal, M.; Venkatachalaiah, K.N.; Kollur, S.P. Dysprosium doped $SrCeO_3$ nanophosphors for advanced photochemical applications: Synthesis, characterization, photo-assisted dye degradation and latent fingerprint visualization. *Materials Science in Semiconductor Processing* **2024**, *182*, 108674, https://doi.org/10.1016/j.mssp.2024.108674.
9. Runčevski, T.; Brown, C.M.The Rietveld Refinement Method: Half of a Century Anniversary. *Crystal Growth & Design* **2021**, *21*, 4821-4822, https://doi.org/10.1021/acs.cgd.1c00854.
10. Landi, S.; Segundo, I.R.;Freitas, E.; Vasilevskiy, M.; Carneiro, J.; Tavares, C.J. Use and misuse of the Kubelka-Munk function to obtain the band gap energy from diffuse reflectance measurements. *Solid State Communications* **2022**, *341*, 114573, https://doi.org/10.1016/j.ssc.2021.114573.
11. Makuła, P.; Pacia, M.; Macyk, W. How To Correctly Determine the Band Gap Energy of Modified Semiconductor Photocatalysts Based on UV–Vis Spectra. *The Journal of Physical Chemistry Letters* **2018**, *9*, 6814-6817, https://doi.org/10.1021/acs.jpclett.8b02892.
12. Das, R.; Choudhary, R.N.P. Electrical and magnetic properties of double perovskite: Y2CoMnO6. *Ceramics International* **2021**, *47*, 439-448, https://doi.org/10.1016/j.ceramint.2020.08.151.
13. Abdullah, M.M. Consequences of frequency and temperature on the ac-conductivity in ε-GaSe semiconductor single crystal. *Results in Physics* **2021**, *25*, 104220, https://doi.org/10.1016/j.rinp.2021.104220.
14. Madhava Rao, M.V. Introduction to Complex Impedance Spectroscopy: An Overview. *Research Trends and Challenges in Physical Science* **2021**, *2*, 11-17, https://doi.org/10.9734/bpi/rtcps/v2/13173D.
15. Amin, M.; Rafique, H.M.; Yousaf, M.; Ramay, S.M.; Atiq, S. Structural and impedance spectroscopic analysis of Sr/Mn modified $BiFeO_3$ multiferroics. *Journal of Materials Science: Materials in Electronics* **2016**, *27*, 11003-11011, https://doi.org/10.1007/s10854-016-5216-8.
16. Roy, A.; Ponnam, A.; Varade, V.; Honnavar, G.V.; Menon, R. Evidence of Lampert Triangle and Jonscher's Double Power Law in Doped Poly(3,4-ethylenedioxythiophene) Devices. *The Journal of Physical Chemistry C* **2023**, *127*, 5502-5512, https://doi.org/10.1021/acs.jpcc.2c07603.
17. Alhamdi, H.W.; Majani, S.S.; Dilliraj, S.; Seal, A.; Nagesh, N.; Shivamallu, S.; Kollur, S.P. Exploring the anticancer potency and photocatalytic efficiency of bio-derived CuO nanoparticles using Moringa oleifera leaf extract. *Results in Chemistry* **2024**, *7*, 101430, https://doi.org/10.1016/j.rechem.2024.101430.
18. Tasisa, Y.E.; Sarma, T.K.; Sahu, T.K.; Krishnaraj, R. Phytosynthesis and characterization of tinoxide nanoparticles (SnO_2-NPs) from *Croton macrostachyus* leaf extract and its application under visible light photocatalytic activities. *Scientific Reports* **2024**, *14*, 10780, https://doi.org/10.1038/s41598-024-60633-2.